HAL open science

Towards a Local In situ X-ray Nano Computed Tomography under Realistic Cycling Conditions for Battery Research

Zeliang Su, Tuan-tu Nguyen, Christophe Le Bourlot, François Cadiou, Arash Jamali, Vincent de Andrade, Alejandro Franco, Arnaud Demortière

To cite this version:

Zeliang Su, Tuan-tu Nguyen, Christophe Le Bourlot, François Cadiou, Arash Jamali, et al.. Towards a Local In situ X-ray Nano Computed Tomography under Realistic Cycling Conditions for Battery Research. Chemistry–Methods, 2022, 2 (5), pp.e202100051. 10.1002/cmtd.202100051 . hal-03842611

HAL Id: hal-03842611

https://u-picardie.hal.science/hal-03842611v1

Submitted on 20 Jun 2023

HAL is a multi-disciplinary open access archive for the deposit and dissemination of scientific research documents, whether they are published or not. The documents may come from teaching and research institutions in France or abroad, or from public or private research centers.

L'archive ouverte pluridisciplinaire **HAL**, est destinée au dépôt et à la diffusion de documents scientifiques de niveau recherche, publiés ou non, émanant des établissements d'enseignement et de recherche français ou étrangers, des laboratoires publics ou privés.

Distributed under a Creative Commons Attribution 4.0 International License

Check for updates

Chemistry—Methods

Full Papers
doi.org/10.1002/cmtd.202100051

Chemistry Europe
European Chemical Societies Publishing

www.chemistrymethods.org

Towards a Local *In situ* X-ray Nano Computed Tomography under Realistic Cycling Conditions for Battery Research

Zeliang Su,[a, b] Tuan-Tu Nguyen,[a, b, c] Christophe Le Bourlot,[d] François Cadiou,[a, b] Arash Jamali,[a, e] Vincent De Andrade,[f] Alejandro A. Franco,[a, b, g, h] and Arnaud Demortière*[a, b, h]

Performing high resolution 3D imaging with transmission X-ray microscopy (TXM) in an in situ battery system is extremely challenging. We show herein a method to conduct an in situ nano-X ray Computed Tomography (nano-XCT) experiment assisted by the in-line phase contrast technique for low Z elements in batteries. A carbon-based O_2-cathode of Li-O_2 battery was used for this investigation and the time-resolved 3D volumes were obtained and successfully reconstructed. Our approach is to perform a nano-XCT by zooming directly into a laser-shaped area not larger than 50 μm in an in-house in situ cell. The rotation axis of the tomography of this cell being parallel to the plan of the electrode, a specific method of preparing the electrode by laser is required. This method is essential in this approach, which allows to minimize the dead angles, align the beam and adjust the focus plan. We have demonstrated in situ observation of the difficult light species, lithium peroxide, in a lithium-oxygen battery. The time-resolved 3D volumes obtained showed a force pushing the analyzed area out of the field of view. This is due to the thickening of the lithium foil during the electrochemical process. Although X-ray Computed-Tomography (XCT) is often considered non-invasive and beneficial for the development of an in situ experiment for battery research, here we discuss the effect of the focused beam at the nanoscale with a focusing X-ray beam. The current contribution opens possibilities of characterization of battery materials by local in situ nano-XCT under realistic cycling conditions.

1. Introduction

X-ray computed tomography (XCT) has recently attracted a lot of interest in the battery field.[1,2] This technique can provide an explicit 3D structure of the material that is absent in microscopic 2D imaging techniques. These 3D structures can be used to characterize properties of the material or as the input of an electrochemical simulation. It is one of the few techniques that helps to underpin the link between material micro-structure and the electrochemistry.[3–8] Nowadays, the combination of XCT and simulation has become a powerful tool for designing and predicting formulation and microstructure[3–5] to improve the battery performance.

Along with the compelling non-invasive property of XCT, in situ/operando experiments can also be deployed to study the kinetics aspects of the material at multiple scales. Up to date, the most intense development of in situ/operando CT experiments for batteries is done with micrometric resolution (μ-CT). Depending on the X-ray source and the sensors, the field of view varies from hundreds of micrometers to tens of millimeters. A Li-ion 18650 Li-ion battery can be directly 3D imaged, observing the thermal safety, electrode aging and

[a] Dr. Z. Su, Dr. T.-T. Nguyen, Dr. F. Cadiou, Dr. A. Jamali, Prof. A. A. Franco, Dr. A. Demortière
Laboratoire de Réactivité et Chimie des Solides (LRCS)
CNRS UMR 7314
Université de Picardie Jules Verne
Hub de l'Energie, 15 Rue Baudelocque
80039 Amiens Cedex (France)
E-mail: arnaud.demortiere@cnrs.fr
[b] Dr. Z. Su, Dr. T.-T. Nguyen, Dr. F. Cadiou, Prof. A. A. Franco, Dr. A. Demortière
Réseau sur le Stockage Electrochimique de l'Energie (RS2E)
CNRS FR 3459
Hub de l'Energie, 15 Rue Baudelocque
80039 Amiens Cedex (France)
[c] Dr. T.-T. Nguyen
Renault Technocentre
78084 Guyancourt (France)
[d] Dr. C. Le Bourlot
Université de Lyon
INSA Lyon, MATEIS
CNRS UMR551
69621 Villeurbanne (France)
[e] Dr. A. Jamali
Plateforme de Microscopie Electronique
Université de Picardie Jules Verne
80039 Amiens (France)
[f] Dr. V. De Andrade
Argonne National Lab
Advanced Photon Sources Beam line, Bldg. 401/Rm A4115
9700 S. Cass Ave., Argonne, IL 60439 (USA)
[g] Prof. A. A. Franco
Institut Universitaire de France
101 Boulevard Saint Michel, 75005 Paris (France)
[h] Prof. A. A. Franco, Dr. A. Demortière
ALISTORE-European Research Institute
CNRS FR 3104
Hub de l'Energie, Rue Baudelocque
80039 Amiens Cedex (France)

Supporting information for this article is available on the WWW under https://doi.org/10.1002/cmtd.202100051

© 2022 The Authors. Published by Wiley-VCH GmbH. This is an open access article under the terms of the Creative Commons Attribution License, which permits use, distribution and reproduction in any medium, provided the original work is properly cited.

© 2022 The Authors. Published by Wiley-VCH GmbH

volume changes during cell-scale cycling.[9,10] For the evolution of materials at the micrometric scale, one can investigate with in-house operando cells during the cycle. These cells are generally cylindrical with walls made of material transparent to X-rays such as PEEK and polyimide polymers. In these studies, the characterized electrode was cut into a small diameter disc to fit the in situ cell and not to bypass the field of view.

Several groups have successfully conducted in situ/operando μ-XCT with phase contrast techniques for Li-sulfur batteries because the sulfur in the cathode exhibits high contrast with other elements.[9–12] Yermukhambetova et al.[9] used Zernike phase contrast, while the Zielke et al.[11] used single distance phase retrieval to enhance the contrast of sulfur. Silicon as an anode in Li-ion battery has also been extensively investigated by in situ experiment on its volume expansion[13–15] during lithiation. Piestch et al.[13] combined XCT and scanning X-ray diffraction techniques to study the 3D lithiation of silicon on a bulk electrode scale. They were able to follow the in-depth profile of the $Li_{15}Si_4$ over time and show the volumetric changes. Vanpeene et al.[14–16] provided evidence of electrode cracking and gas release due to SEI formation using in situ XCT. Additionally, the in situ XCT has also been found particularly useful for interface detachment studies of all-solid-state battery.[17] Several studies[18–20] have employed in situ XCT experiments at nanoscale resolution with different cell designs. Wang et al.[18,19] visualized several Sn particles in time-resolved and in high resolution during lithiation and sodiation in an capillary cell, while Li et al.[20] visualized with in situ nano-XCT the (de)lithiation of primary germanium particles in a quartz in situ cell.

Over the last decades, many interests have been brought in metal-O_2 batteries due to their high energy densities.[21,22] The operation of these batteries is associated with the deposition and formation of metal oxides during cycling. For instance, the products of sodium oxides and tin oxides in Na-O_2[23] and Zin-O_2[24–26] batteries are micrometer-sized and exhibit high X-ray contrast with a carbon matrix, making XCT a relevant and robust technique for characterization. Manke et al.[25] visualized *operando* the transition from Zn to ZnO. They also compared the measured volume variations with the theoretical one. This group also conducted the in situ XCT on lithium for the Li-O_2 battery.[27] They put forward with the time-resolved 3D observation an irreversible formation of a transition layer on the lithium surface. This formed porous transition layer is mainly composed of LiOH and Li_2CO_3, which is formed by the presence of oxygen and the degradation of glyme-based electrolyte. Thanks to the time-resolved CT experiment, they found it thickened during cycling and attributed it to the poor reversibility. They pointed out that this is a hidden factor that is often ignored in the field of Li-O_2 battery (LOB) and other metal-air batteries but has severe consequences for the cyclability. On the cathode side, the size of the products and the material are on sub-micrometer scale and the contrast is quite low in pure absorption. The resolution and contrast of the micro-XCT absorption applied in their study are not adequate to capture the products in the O_2-cathode. In our previous study,[28] we have investigated the phase contrast 3D imaging for enhancing the contrast of a cycled LOB cathode material and extracting its tortuosity and porosity. To meet the challenge of 3D imaging the products in a LOB cathode via an in situ system, we integrate our previous in-line Zernike Phase Contrast nano-CT method[28] into a new in situ XCT cell design.

In the current contribution, we report a novel approach to conduct in situ nano-XCT experiment for the Li-O_2 battery using an in-house electrochemical cell. A specific laser sample preparation was used to allow alignment between the beam and the focusing plan on an acquisition area, which does not exceed 60 μm. Zernike phase contrast was applied to enhance the contrast of Li_2O_2. The tomography acquisition and reconstruction with limited angles will be detailed. The spatial resolution reached 360 nm. The effect of the X-ray beam on electrochemistry is discussed, and potential ways for improvement for this experiment are then proposed. The time-resolved 3D volumes obtained during the discharge were injected into a particle tracking algorithm to study the motion of the formed particles.

Experimental Methodology

Cell Design

The design of cells for X-ray tomography is the most essential part and will influence how the nano-CT experiment is carried in situ. There are several constraints related to the design of a nano-XCT cell. First, dead angles obscuring X-rays in the field of view (FoV) during the rotation should be limited. Dead angles can degrade the quality of the reconstruction, resulting in bifurcated streak artifacts that appear[29–33] on small objects and high curvature edges. These artifacts can be easily identified because they have an identical orientation in the tomographic reconstruction plan (XY plan in Figure 1a) and throughout the stack. It has been reported that numerical reconstructions such as total variation reconstruction (TV)[29] as well as a coupling of emerging reconstruction algorithms with machine learning assisted in-painting techniques[30–33] can help mitigate these artifacts. Second, the X-ray absorbance of the components and their thickness should be controlled. Polyether ketone, polyimide, glassy carbon (GC), and berylium are often chosen for the main body or for the X-ray transparent window of the X-ray cell in the literature.[2,34] The thickness of the overall cross-

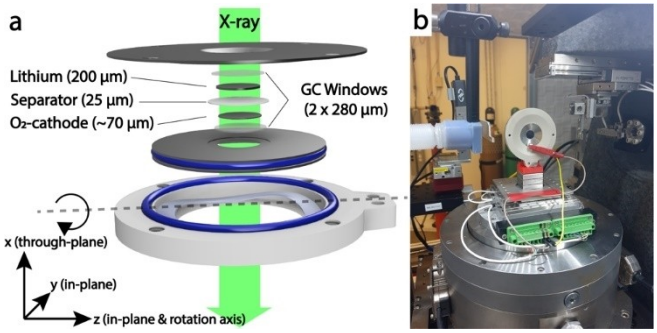

Figure 1. Tu-cell and beam-line integration (a) A sketch of the Tu-cell and its components with the conventional axis throughout this work. (b) Image of the Tu-cell seated and connected to the rotation stage in the ID-32-C APS beamline. The red part under Tu-cell is a customized 3D printed component that can be personalized for adapting different beamlines.

© 2022 The Authors. Published by Wiley-VCH GmbH

26289725, 2022, 5, Downloaded from https://chemistry-europe.onlinelibrary.wiley.com/doi/10.1002/cmtd.202100051 by Université De Toulouse 3, Wiley Online Library on [20/06/2023]. See the Terms and Conditions (https://onlinelibrary.wiley.com/terms-and-conditions) on Wiley Online Library for rules of use; OA articles are governed by the applicable Creative Commons License

section is critical in nano-XCT. We used simulators[35–37] to help estimate X-ray transmission and conceive the electrode thickness before performing the in situ nano-XCT experiment. Third, the difficulty of assembling cell must be taken into account. Deposition/coating[9,16,20] on a tip or mechanical shaping[14,16,18,19,27] are two common strategies in the literature for preparing materials for in situ XCT cells. Our method is different, which is to use a laser to cut patterns into the electrodes (see the section on Laser sample preparation and beam alignment). The following in-house disc geometry cell, TU-cell, allows electrochemical measurements to be conducted with realistically sized electrodes (Figure 1).

Tu-cell is designed with a flat, slim geometry and an inherently 30° of dead angles. It is made up of three parts (Figure 1a): a large stainless-steel cover (LSS), a movable stainless-steel (SS) disc in the middle and a Teflon base. The cover and the base are static, while the middle part is movable and compressed by a spring. Air tightness is ensured by two PEEK polymer rings compressed around the central disc and the Teflon base. Glassy carbon (GC) windows are glued, by a silver epoxy resin for the electronic conductivity, to the hollow indentation in the center of both the SS disc and the cover. To avoid direct contact between electrolyte and silver epoxy, the spaces between the GC window and the LSS disc are coated with a chemically resistant silicate epoxy. Figure 1b shows the way that Tu-cell is integrated on the ID-32-C beamline of the APS synchrotron.

Materials and Synthesis

The lithium pellets were purchased from MSESupplie and the glassy carbon window from HTW Hochtemperatur-Werkstoffe GmbH. The separator is Celgard industrial grade and the self-standing binder-free carbon O_2-cathode is made of raw MWCNT from the NanoTech Lab®. To produce this CNT electrode, the MWCNT is first dispersed with isopropanol in a ratio of 12 mg/L with 1 h of ultrasonication. This solution is then filtrated through a Whatman glassy fiber filter with a pore size of 1.2 μm until a loading electrode disc of 1.69 mg/cm^2 is obtained. The dispersed MWCNT has been retained on the filter and forms an entangled network. During the loading, the carbon paper made of entangled MWCNT is self-contained and can be easily peeled off the filter using tweezers. Its thickness is approximately 65 μm, roughly equal to the width of the FoV of the ID-32 TXM. The electrode is treated with chloric acid (~9% volume ratio) for 1 h to reduce residual iron. During the treatment, a vacuum is made above the solution to extract the bubbles trapped in the porosity for better acid impregnation. It is then washed by abundant deionized water and ethanol before being dried in a vacuum oven for at least 2 h at 120 °C. The electrolyte we used is 2 M $LiNO_3$ in dimethylacetamide as described by Lepoivre et al..[38] The electrolyte was dried and stored with an activated molecular sieve. Before the in situ experiment, it was bubbled in a vial with a syringe connected to a balloon filled with pure oxygen for about 30 min.

Laser Sample Preparation and Beam Alignment

The laser is frequently used to sculpt tiny pillars (a few tens of μm in diameter, which are as thin as a hair) for the ex situ nano-XCT.[39] However, it is not easy to use such a tiny tip in an in situ cell and mount it in the glovebox. The small amount of active material can also raise problems of reproducibility in electrochemistry, because it is difficult to control the mass loaded on the tip as well as to estimate a current. To remedy this, the experiment was conducted differently. The following laser top-down approach can use the same electrode size as in a coin-cell or Swagelok and apply the same current density.

We used the laser (Zeiss Palm laser micro-dissector) to cut patterns on the electrode in order to (1) reduce dead angles and (2) align the beam and the focus plan. On the 14 mm diameter CNT electrode, we removed three squares (Figure 2a) with a side length of at least 5 times FoV (~250 μm) around the acquisition area (A_{acq}). The tomography A_{acq} is the small pillar between the two upper squares. As the axis of rotation of the Tu-cell is parallel to the plan of the electrodes, the X-rays pass through all the battery components. Details of the lithium and the separator were also imaged with the cathode in the parallel beam mode (Figure 2a, Figures S1 and S2 in Supporting Information).

Figure 2d shows the comparison of the theoretical transmission from different angles by removing (blue curve) and without removing the materials around the A_{acq} (other colors). Various absorbent materials (expressed as % by X-ray cross-sectional width) without laser cutting are plotted. We see that the transmission decreases with the angle of rotation θ when the thickness increases as a function of 1/cosθ. A 5% material per X-ray cross-section equivalent to a field of view will lose 40% transmission at ±50°. And the aperture narrows further to ±25° with 18%/FoV absorbance cross-sectional material. In practice, a transmission greater than 60% gives a better quality of reconstruction as indicated by the dotted line in Figure 2d. Other parameters such as the beam energy and the thickness of the different components should be adjusted accordingly for better transmission.

Regarding the assembly of the Tu-cell, it is as easy as mounting a coin-cell battery. The squares are barely visible to the naked eye. The third square at the bottom right is not mandatory. But it increases the visibility and guide to vertically align the tiny pillar according to the vertical axis of the microscope. While mounting the cell, the pillar must be aligned with the corner, which has two holes for screws at the bottom of the Tu-cell that indicates the z direction. In a glove-bag filled with pure oxygen, we simply started by putting the O_2-cathode and then the Celgard separator on the LSS disc. Addition of 100 μL of electrolyte pre-bubbled with oxygen wets the Celgard and the cathode. And finally, we ended up stacking neatly the lithium foil on top and closing the cell carefully with screws.

After the assembly, finding A_{acq} in TXM and aligning beam and focus is a decisive step in Tu-cell. As shown in Figure 2a and Figure S1, the squares are rather transparent, but they can be recognized by their noticeable shape. The weight of the materials removed from the squares is negligible (much less than 0.1 mg) compared to the entire X-ray window and the whole O_2-cathode. To increase the chances of finding the pattern under the microscope and limit the duration of the X-ray irradiation, dozens of these patterns separated by 1 to 2 mm were cut in the center of the electrode. These patterns were used to move the center of rotation on the A_{acq}. For this, we scrutinized a position on the through plan direction for the Tu-cell such that the dark pillar remains in the center of the camera while rotating the cell (Figure 2c). A quick shutter for the beam is mandatory during the above pattern search and position adjustment on the x-axis to minimize the X-ray dose. Note that the effective aperture angles will also be close to the theoretical one (±75°) if the A_{acq} is at the center of the transmission window. In this work, an effective opening of −67° to +67° was obtained.

Electrochemistry and Zernike Phase Contrast

On the beamline, the electrochemical measurement was done with a potentiostat SP-200 of Bio-logic. We imposed galvanostatic pulses of 5 μA in the Tu-cell, which is equivalent to a current density of 0.004 mA/cm^2 (four-fold less as in a Swagelok) and ~C/15 of C-rate of the self-standing cathode in Tu-cell configuration.

© 2022 The Authors. Published by Wiley-VCH GmbH

26289725, 2022, 5, Downloaded from https://chemistry-europe.onlinelibrary.wiley.com/doi/10.1002/cmtd.202100051 by Université De Toulouse 3, Wiley Online Library on [20/06/2023]. See the Terms and Conditions (https://onlinelibrary.wiley.com/terms-and-conditions) on Wiley Online Library for rules of use; OA articles are governed by the applicable Creative Commons License

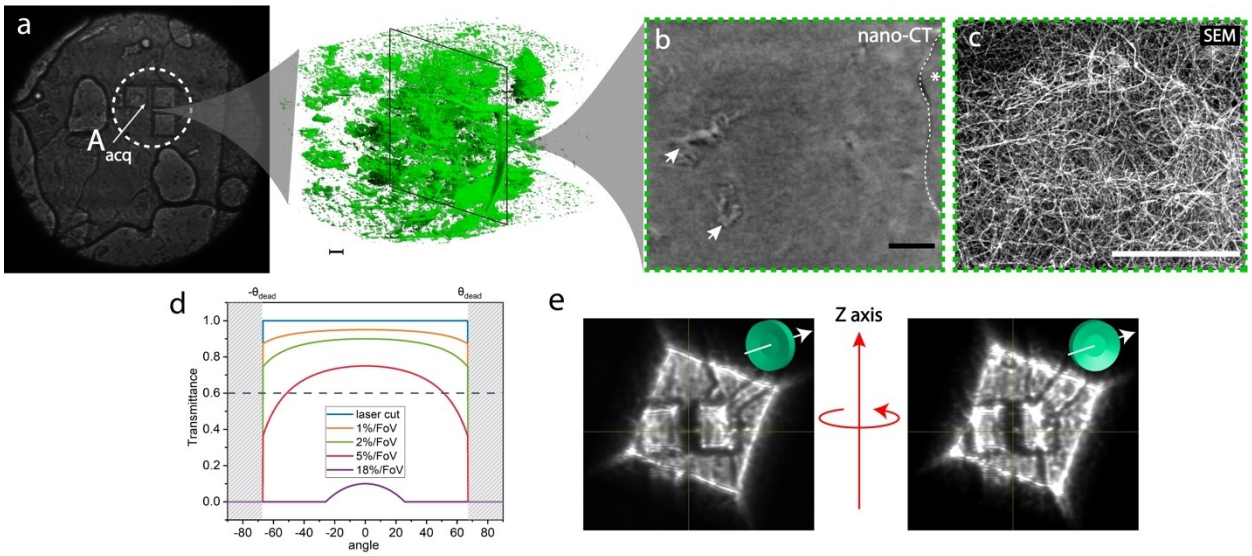

Figure 2. Illustration of beam and focus alignment (a) the laser cut patterns in the X-ray beam in parallel beam mode (low resolution without magnification). The white dotted line circle highlights the patterns of squares cut by laser. And the acquisition area (A_{acq}) is the pillar between the two top squares. (b) The green volume shows the A_{acq} of the pristine material with pores and fibrils roughly segmented, and an ortho-slice of the raw CT volume. The asterisks spot the outside void cut by laser of the electrode. And the arrows point out the macro-pores in the material. (c) an SEM image of this material is shown on the side. The scale bars of (a–c) are 5 μm. (d) a simulated transmission rotation angle plot of Tu-cell with/without the laser-abraded assuming an homogeneous background. 0° corresponds to the through-plan x axis perpendicular to the plan of electrodes. Several examples of transmission without laser-cutting for materials of different absorbance in between 1–18% normalized by field of view (FoV) are also shown. The minimum transmission of 60% for good tomography quality is indicated by a dashed line (e) illustration on how to bring the center of rotation onto the A_{acq}. Two pictures of well aligned Tu-cell at 0° and 15° in the parallel beam mode are shown. When the focus plan is precisely on the carbon cathode, not on the lithium nor on the separator, the dark laser-shaped pillar should not deviate from the center of camera.

In this experiment at 32-ID-C APS, a zone plate condenser, an in-line Zernike phase ring, 8 keV energy, and a working distance of 3.4 m were used, which provides a voxel size of 27 nm. The acquisitions were made during the relaxation periods marked by the dashed line in Figure 3a. 721 projections of one second of exposure have been collected using a scintillator (LuAG CCD) coupled with a CCD camera (Grasshopper3 5.0 MP GS3-U3-51S5M-C) in the effective aperture of 134°. The gold phase ring was placed downstream to the sample to induce Zernike Phase Contrast, which enhances the contrast of light elements. Figure S4 shows a comparison of the same projection between the absorption and phase contrast mode of TXM. The edges of the relief and a few small features have been emphasized by the Zernike phase contrast. All components are in compression, therefore steady and motionless CT acquisition can be achieved in Tu-cell.

Other Postmortem Sample Preparations

The postmortem characterization samples were first washed with dimethylacetamide solvent in a dry room at less than 50 ppm humidity for at least 30 min to dissolve the salt. It is then transferred through a stainless-steel sample holder for SEM to avoid contamination from air and moisture. For the ex situ XCT, the CNT electrode was discharged at a current density of 20 μA/mg. A small piece of electrode was withdrawn by an epoxy wetted graphite tip and sealed in a Kapton tube in the dry room. 1200 projections were collected within 180° degree. The TEM sample preparation was also performed in the dry room. In a mortar, we added few drops of dimethylacetamide with a piece of discharged cathode and then grinded the mixture. We withdrew a drop of solution from the mortar with a pipette and deposited it on a TEM grid. It was then put onto the TEM sample holder and transferred within a bag filled with argon.

2. Results and Discussions

2.1. Reconstructed Volumes and the Segmentation

The projections background brightness in the range of aperture angles may vary. This is due to the uneven thickness of other components, such as lithium and the separator, the X-ray beam crosses. Second, the overall transmission decreases slightly in the last few angles before the dark out of dead angles. Normalization by the average value of each projection can easily correct these problems of overall variation in brightness and improve the reconstruction.

The projections were reconstructed using the filtered back propagation in TomoPy[40] python package and filtered back by a kernel three 3D median filter. Six volumes on the characteristic discharge plateau were obtained. The depth of focus was 140 μm, which makes it possible to see the streaks and textures of the surface of the lithium and of the separator (shown in Figure S5 or in Video Supporting Information SV1). These features scroll quickly in the background during rotation and are not captured by the reconstruction algorithm. Highly transparent spots in the foreground can still be correctly reconstructed into 3D contrasted particles (in Figure 3b or Figure S5).

The scissor-shaped missing angle artifacts can be seen on the high curvature surface in the reconstruction plan (top view in Figure S5b), leaving bright gratings in the side and front views of Figure S5b and as evidenced by the circles in Figure S5c. These scissors like artifacts form 67° angles with the

© 2022 The Authors. Published by Wiley-VCH GmbH

26289725, 2022, 5, Downloaded from https://chemistry-europe.onlinelibrary.wiley.com/doi/10.1002/cmtd.202100051 by Université De Toulouse 3, Wiley Online Library on [20/06/2023]. See the Terms and Conditions (https://onlinelibrary.wiley.com/terms-and-conditions) on Wiley Online Library for rules of use; OA articles are governed by the applicable Creative Commons License

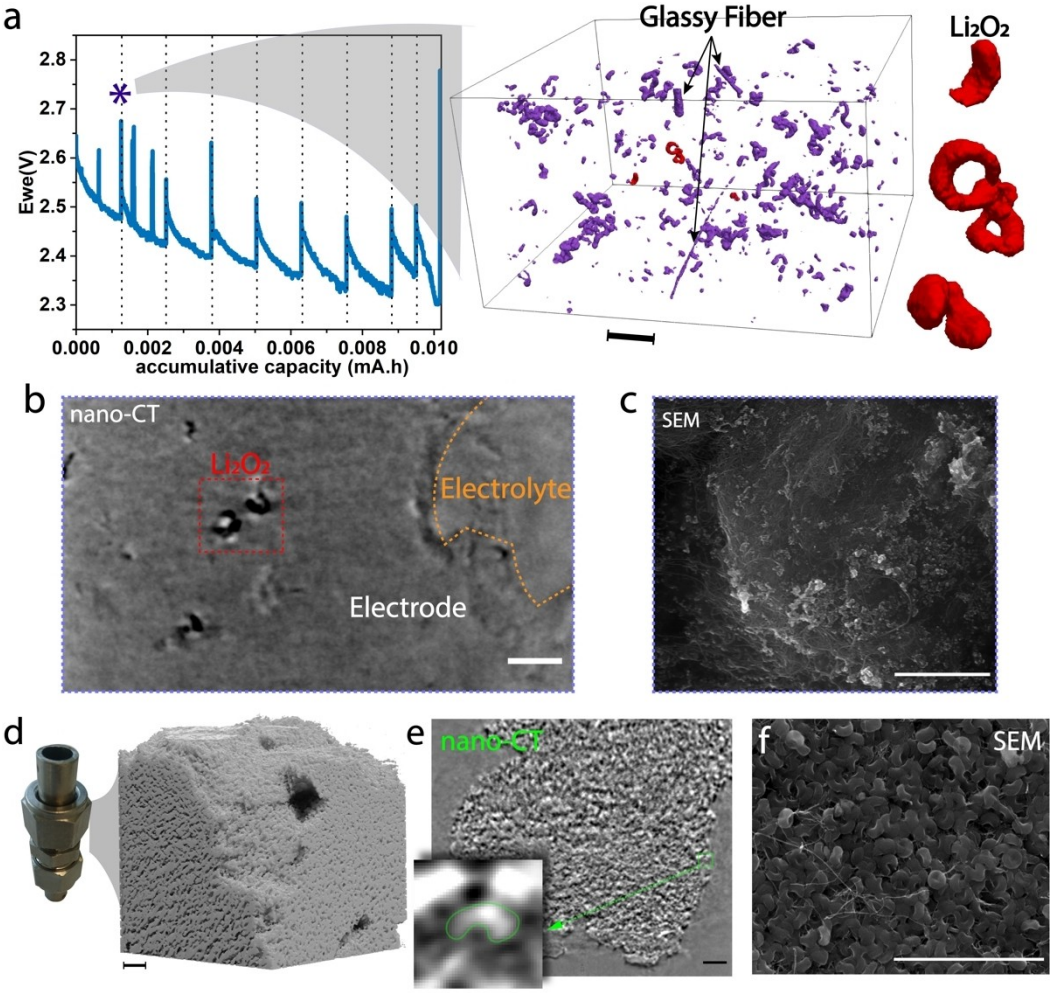

Figure 3. Comparison of in situ and ex situ volumes. (a) The graph shows the discharge curve of the Tu-cell. The dashed lines indicate the relaxation phase where the tomographic acquisitions were made. On the top-right corner, a 3D rendering of the segmentation of the first in situ volume after 20 minutes of discharge. Three particles in the volume are highlighted in red. (b) is a cross-section of this volume. (c) a post-mortem SEM images of the cell. (d) a digital image of a Swagelok LOB and the rendering of an ex situ CNT cathode filled with lithium peroxide. (e) A raw slice of the volume (d). The inset zoom is from the red rectangle at the right border of the material, in which we see one of the peroxide toroid laid parallel to the plan of the image. (f) the SEM image of this discharged electrode. All scale bars in this figure represent 5 μm.

x and y axis, which correspond to the dead angles. They will be absent from the side and front views because of the delay effect. In other words, a particle's bright artifacts will appear as noise in another slice when we observe them in the side and front view. Thus, we choose a 2D segmentation performed in the side views to be less influenced by such artifacts.

The other time-resolved volumes are segmented together by the convolutional neural network (CNN) in SegmentPy software.[41] To do this, three raw reconstruction slices in each volume are retrieved for training the network, which is in total eighteen images for six volumes in discharge. Eighteen out of the thirty pairs of raw/segmentation samples at different time steps have been placed in the training dataset and the other twelve are divided into validation and testing datasets. The lithium peroxides, other dark fibers (broken fragments of glassy fiber from the synthesis) and the electrolyte front have all been segmented into a single phase. The CNTs appears as a noisy shadow due to the resolution (in Figure 1b and 3b) and are not able to be segmented here. The scores of the CNN trained for segmentation can be found in Figure S6.

Dark particles appear starting with the first discharge volume. In general, they have a high contrast in the dark colors shown in the raw tomograms Figure 3b with the Zernike phase contrast. They are segmented into purple phases rendered in 3D in Figure 3a. These particles have different morphologies such as sphere and toroid. A few large fiber fragments can also be seen. The fibrils are actually broken fragments from the glass fiber filter that we use to make the self-standing carbon nanotube electrode (see section 2.2). The dark particles are the lithium peroxide formed in the first step and the other white particles are impurities which remain from the pristine state. It can be seen from the red inset particles on the right of Figure 3a that some are in incomplete shapes closed to semi-spheres and some are aggregates of toroid and sphere, (also in Figure S5b and 5c). This suggests that at the beginning of Li_2O_2

© 2022 The Authors. Published by Wiley-VCH GmbH

26289725, 2022, 5, Downloaded from https://chemistry-europe.onlinelibrary.wiley.com/doi/10.1002/cmtd.202100051 by Université De Toulouse 3, Wiley Online Library on [20/06/2023]. See the Terms and Conditions (https://onlinelibrary.wiley.com/terms-and-conditions) on Wiley Online Library for rules of use; OA articles are governed by the applicable Creative Commons License

germination, peroxides do not grow simultaneously and not at the same rate.

2.2. Oxygen Limitation and Beam Effect: Ex situ vs. in situ Nano-XCT

Figure 3 compares the in situ discharged volumes in the Tu-cell and an ex situ volume in a pressure controlled Swagelok system described in Lepoivre et al..[38] The formation of Li_2O_2 in the Tu-cell (Figure 3b is rather scarce. The ex situ volume of control experiment in Figure 3d was retrieved from another CNT cathode in the same batch discharged at a current density of 20 mA/g and ending at the cut-off voltage of 2 V (for the sample preparation, see above). 70% of this volume is filled by peroxides. From the cross section and the SEM image, we see that the peroxides in Tu-cell are in a primary state of aggregation. Confirmation by post-mortem TEM/EDX (sample preparation above) of the Li_2O_2 formation was performed in both ex situ and in situ (Figure S8 and S9). Some peroxide particles (in Figure 3a) are in uncompleted round shapes compared to the toroid-like peroxide formed in a Swagelok (in Figure 3d). There could be several reasons for the limited growth of Li_2O_2 in A_{acq}.

First, the Tu-cell is a closed system. It was mounted in 1 atm of pure oxygen and the amount of oxygen depends on the interior volume of the Tu-cell spaced by the stack of electrodes (Figure 1). It is estimated to be less than 1 mL (considering the thickness of the electrodes and the diameter of the LSS disc), unlike the 10 mL of the Swagelok configuration used in this study. The oxygen reduction plateau of oxygen reduction in Tu-cell is thus shorter.

The oxygen diffusion path is the second limited factor in chocking the growth of early germinated particles. In a typical Li-O_2 battery (Figure 3d), the direction of the oxygen diffusion is normal to the plan of the electrode. In the Tu-cell, oxygen must travel radially from the outside of the electrode disc to the center in order to reach the reaction point. A_{acq} is in the center of the electrode, approximately 5.6 mm away from the edge of the electrode. In-plan oxygen diffusion is in a millimeter range in the Tu-cell which contrasted with in-plan diffusion of the micrometer range in a typical Swagelok. Local oxygen depletion of A_{acq} was probably the cause of the hindrance as a result of the reaction. To shorten the oxygen diffusion distance to A_{acq}, a potential improvement in the experiment could be to split the electrode in half so that the central A_{acq} is exposed at the border and closer to the oxygen (A_{acq} should still position in the middle of the transmission window for the opening window).

Besides the limited amount and the long diffusion path of the oxygen, the beam effect could be another factor hindering the reaction. Although X-ray CT techniques are often considered non-invasive, in TXM mode, where the beam is focused and the photon flux is strongly condensed on the tiny A_{acq}, the impact of the beam should not be overlooked.

Here we use the CNT binder-free cathode that can (a) avoid dissociation of the binders in the electrolyte by the heat on the beam and the presence of organic solvent (the polymer chain starts to move above the temperature of glass transition). (b) exclude the side reaction between the peroxide and the polymers for the simplicity of the involved reactions.

A fast shutter was used throughout this study to reduce X-ray irradiation to the in situ system and the shutter was only open when acquiring the CT scan and looking for patterns before the acquisitions. Nevertheless, the beam did impact the electrolyte. Both in parallel beam mode and in the TXM. First, in parallel mode without magnification, bubbles are created (Figure S2) and moved after several shutter opening plans at the same location. Second, with the converged nano-XCT beam onto the A_{acq}, a gas-liquid interphase in the northeast corner of the reconstructed volumes appears (Supporting Video SV1). During the discharge, this interface gradually propagates towards the center of the cube, indicating that the amount of electrolyte is decreasing in A_{acq}. Interestingly, we noticed that a brownish product and a strong-smelling gas formed after experiment. This is typically the NO_2 of the lithium nitrate salt as described in the original article on this electrolyte.[42] Two Tu-cells were cycled under identical condition in the beam and outside the beam. We see that in Figure 3a or Figure S3 the beam clearly induced noises on the plateau and a higher polarization of about 100 mV. Notably, several spikes, might be also due to the beam, appeared at the beginning of the plateau during the galvanostatic pulses while the shutter is closed.

2.3. Particle Tracking in Subsequent Time Steps

After the segmentation step on the obtained volumes, different types of features are extracted: particles, inclusions, residual glassy fibrils, and liquid-gas interface. The segmented volumes are labelled (a unique identifier is given to each feature) and a set of properties is measured: including barycenter, volume, area, inertia matrix, main axis, sphericity. These analyses are performed for each tomographic volume. From this recovered data set, a tracking algorithm is established to connect features from one time step to another, based on discrete correlation method, in order to construct the tracks. To do this, a probability graph is built on the likelihood for each pair of features in an adjacent time step based on physical laws, geometric considerations and other compatibility criteria. Once the graph is constructed, the tracks are extracted using a shortest path algorithm, connecting each individual particle through the time axis. A track gives the trajectory of each individual particle and the evolution of its properties.

In Figure 4a, the displacement vectors between time steps given by these tracks for each particle are shown (from dark colors to bright colors). It should be noted that the Tu-cell rests firmly on the stage by the attraction of magnets and that the cables rotate with the stage (Figure 1b), so no external force is causing these displacements. The evolution of the volume over time is shown in the SV1 video. In this video, we see that the particles are moving roughly in the same direction, taking a big step at first in the x axis direction, then small displacements in the following steps. This is illustrated by the arrows in Figure 4a1 and the polar graph Figure 4b1. We see that these

© 2022 The Authors. Published by Wiley-VCH GmbH

26289725, 2022, 5, Downloaded from https://chemistry-europe.onlinelibrary.wiley.com/doi/10.1002/cmtd.202100051 by Université De Toulouse 3, Wiley Online Library on [20/06/2023]. See the Terms and Conditions (https://onlinelibrary.wiley.com/terms-and-conditions) on Wiley Online Library for rules of use; OA articles are governed by the applicable Creative Commons License

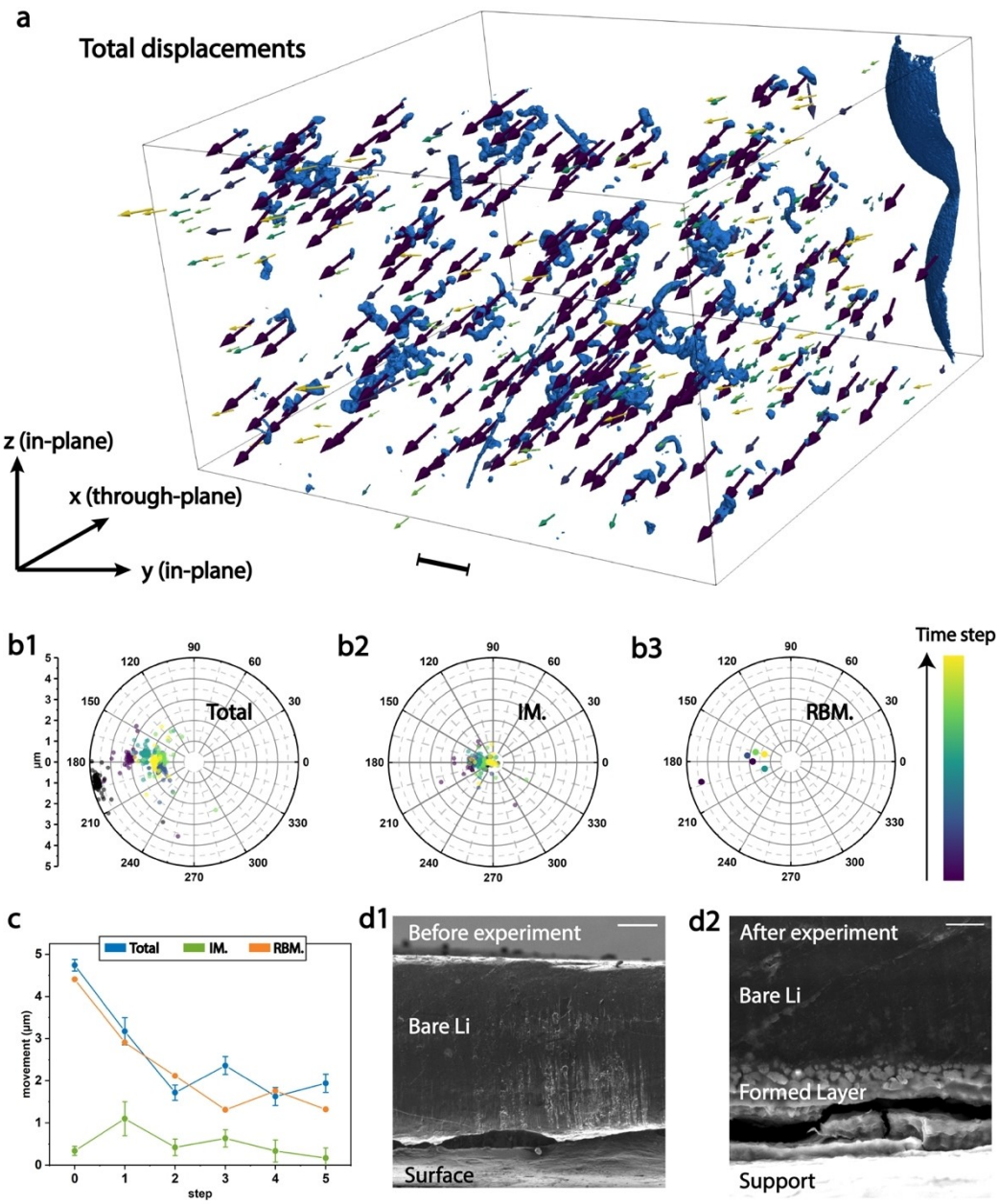

Figure 4. Dynamics study of the time-resolved volumes (a) The 3D rendering of tracked total displacements (rigid body movement RBM + intra-particle movement IM) for all the particles in time steps. The size of arrows indicates the magnitude of movement, and its color indicates the time step. And the time step color bar is shared between the (a) and (b) plots. The scale bar in (a) From left to right, b1-3) are respectively polar plots for total displacements, RBM, and IM projected on the plan XY (the movements on z direction are quasi-null), showing the distribution of motion vectors for each tracked particle at time t. The latitudes represent angle formed between the vector and the x axis at plan XY, and the longitude its module of the vector. c) plot of average module of displacement for all tracked particles with time. d1-2) SEM images comparison of the intersection of the pristine lithium foil and the post-experiment one. A thick non-uniform micrometric layer is formed on the surface of Li. The scalar bar in d1 represents 100 µm, and 20 µm for d2.

movements are in the micrometer range (tens of voxels in Figure 4c), while the precision of the machine is in the nanometric range. These shifts clearly do not come from the machine but from real steric changes within the battery.

We can divide the total displacements into a single directional monotonic rigid body motion (Figure S9 and Figure 4b2 RBM) and an interparticle motion (Figure S9 and Figure 4b3). The RBM indicates that a force is applied globally on the A_{acq}. Here, the direction of this force points to the negative direction of the x, y axis on the horizontal plan. Note that the separator and lithium are in the positive direction of the x axis and the GC window on the negative side. We figured out that the origin of this force is in fact the formation of a cumulative porous transition layer formed on top of the lithium during cycling. This formation was highlighted in two other micro-CT studies of lithium for LOB.[27,43] The magnitude of RBM measured here is in the micrometer range that is in consistence with these studies. We further confirmed the presence of this transition layer by

© 2022 The Authors. Published by Wiley-VCH GmbH

26289725, 2022, 5, Downloaded from https://chemistry-europe.onlinelibrary.wiley.com/doi/10.1002/cmtd.202100051 by Université De Toulouse 3, Wiley Online Library on [20/06/2023]. See the Terms and Conditions (https://onlinelibrary.wiley.com/terms-and-conditions) on Wiley Online Library for rules of use; OA articles are governed by the applicable Creative Commons License

postmortem SEM (Figure 4d1 and 4d2) on the cross section of the discharged lithium in the Tu-cell. The composition of this layer is mainly nitrate and oxide, according to the EDS spectrum given in Figure S10. Indeed, the O_2-cathode is placed on the movable LSS disc (Figure 1a). The cathode is gradually pushed out of the FoV during the formation of the transition layer. Our experiment involves only the beginning of the first cycle, the reversibility of this transition layer formed in the electrolyte should be investigated in the future.

Interparticle motions (IMs), on the other hand, is used to assess local stresses between particles and indirectly reflect the changes in CNT matrix during the discharge. Figure 4b3 shows that the IMs of the peroxide particles formed are on average half of the RBM and the directions do not exceed a fan of 30° around the RBMs direction. IMs are thus small in this work, and no obvious shear and expansion forces were observed to tear the bulky electrode in A_{acq} due to the reactions. We can also see from Figure 4c that the first step of total displacement and RBM is substantial, then tend to stabilize at around 1.5 μm per step. This suggests that the growth rate of this layer is higher at the beginning and then slows down due to the oxygen depletion and accessibility of the bare lithium surface.

Dynamics study of the time-resolved volumes (a) The 3D rendering of tracked total displacements (rigid body movement RBM + intra-particle movement IM) for all the particles in time steps. The size of arrows indicates the magnitude of movement, and its color indicates the time step. And the time step color bar is shared between the (a) and (b) plots. The scale bar in (a) From left to right, b1-3) are respectively polar plots for total displacements, RBM, and IM projected on the plan XY (the movements on z direction are quasi-null), showing the distribution of motion vectors for each tracked particle at time t. The latitudes represent angle formed between the vector and the x axis at plan XY, and the longitude its module of the vector. c) plot of average module of displacement for all tracked particles with time. d1-2) SEM images comparison of the intersection of the pristine lithium foil and the post-experiment one. A thick non-uniform micrometric layer is formed on the surface of Li. The scalar bar in d1 represents 100 μm, and 20 μm for d2.

3. Summary and Outlook

The current study has pushed forward the challenging development of the in situ nano-XCT experiment for lithium batteries. We have demonstrated the feasibility of high-resolution local tomography using the Zernike Phase Contrast for a low contrast Li-O_2 cathode. A carbon nanotube based O_2-cathode was used throughout this study and the nanotube matrix is almost visible. We have presented the in-house Tu-cell, which has the advantages of easy cell assembly and a good reproducibility in terms of electrochemistry. Specific laser sample preparation is required for beam alignment and allow the adjustment of the focus plan. The in situ volumes are compared to the ex situ results, where Li_2O_2 is massively formed. We have also discussed the important factors that can influence the quality of the operando tomography. By analyzing the resulting volumes, the growth of Li_2O_2 was found to be choked at the beginning of the in situ experiment. Several explanations have been given (a) long diffusion path of O_2 to A_{acq}, (b) local evaporation of the electrolyte due to the X-ray beam and (c) the lack of oxygen in the airtight design of the operando cell. Besides, we found that the formed lithium peroxide particles did not separate from each other which suggests that there is no local steric expansion or shrinkage. However, they all move roughly parallel in the same direction with each time step, suggesting an external force being applied to the A_{acq}.

Based on the current findings, it would be necessary in the future work to add a gas outlet which can be connected to the rotation stage to extend the oxygen tank and obtain a longer plateau. In addition, the choice of electrolyte or the shape of the laser cutting pattern could be rethought. A less volatile electrolyte such as the long chain glymes or the ionic liquid and a more stable salt can replace in this experiment the DMA and $LiNO_3$. The laser-shaped pattern could have a more irregular and larger shape to facilitate the pattern searching in parallel beam mode. Higher X-ray energy can be used for higher transmission and less interaction between electrolyte and beam. The current results are particularly important as they have opened up the possibility of conducting a local in situ nano-XCT using real world electrodes, an exact amount of electrolyte and realistic cycling conditions. The results of this investigation can also be generalized to other battery systems. Other advanced battery materials can be beneficial and fitted in Tu-cell using the method of laser preparation and time-resolved 3D imaging.

Conflict of Interest

The authors declare no conflict of interest.

Keywords: electrochemical in situ · nano-CT · Zernike phase contrast · Li-air battery

[1] P. Pietsch, V. Wood, *Annu. Rev. Mater. Res.* **2017**, *47*, 451.
[2] S.-M. Bak, *NPG Asia Materials* **2018** *18*, 563.
[3] X. Lu, A. Bertei, D. P. Finegan, C. Tan, S. R. Daemi, J. S. Weaving, K. B. O'Regan, T. M. M. Heenan, G. Hinds, E. Kendrick, D. J. L. Brett, P. R. Shearing, *Nat. Commun.* **2020**, *11*. 2079.
[4] T.-T. Nguyen, A. Demortière, B. Fleutot, B. Delobel, C. Delacourt, S. J. Cooper, *Npj Comput. Mater.* **2020**, *6*.123.
[5] J. Landesfeind, M. Ebner, A. Eldiven, V. Wood, H. A. Gasteiger, *J. Electrochem. Soc.* **2018**, *165*, A469.
[6] M. Ebner, D.-W. Chung, R. E. García, V. Wood, *Adv. Energy Mater.* **2014**, *4*, 1301278 .
[7] X. Lu, S. R. Daemi, A. Bertei, M. D. R. Kok, K. B. O'Regan, L. Rasha, J. Park, G. Hinds, E. Kendrick, D. J. L. Brett, P. R. Shearing, *Joule* **2020**, *4*, 2746.
[8] T. Nguyen, J. Villanova, Z. Su, R. Tucoulou, B. Fleutot, B. Delobel, C. Delacourt, A. Demortière, *Adv. Energy Mater.* **2021** 2003529.
[9] A. Yermukhambetova, C. Tan, S. R. Daemi, Z. Bakenov, J. A. Darr, D. J. L. Brett, P. R. Shearing, *Sci. Rep.* **2016** *6*. 35291.
[10] C. Tan, T. M. M. Heenan, R. F. Ziesche, S. R. Daemi, J. Hack, M. Maier, S. Marathe, C. Rau, D. J. L. Brett, P. R. Shearing, *ACS Appl. Energy Mater.* **2018**, *1*, 5090.
[11] L. Zielke, C. Barchasz, S. Waluś, F. Alloin, J.-C. Leprêtre, A. Spettl, V. Schmidt, A. Hilger, I. Manke, J. Banhart, R. Zengerle, S. Thiele, *Sci. Rep.* **2015**, *5*, 10921.

© 2022 The Authors. Published by Wiley-VCH GmbH

26289725, 2022, 5, Downloaded from https://chemistry-europe.onlinelibrary.wiley.com/doi/10.1002/cmtd.202100051 by Université De Toulouse 3, Wiley Online Library on [20/06/2023]. See the Terms and Conditions (https://onlinelibrary.wiley.com/terms-and-conditions) on Wiley Online Library for rules of use; OA articles are governed by the applicable Creative Commons License

[12] G. Tonin, G. Vaughan, R. Bouchet, F. Alloin, M. Di Michiel, L. Boutafa, J.-F. Colin, C. Barchasz, *Sci. Rep.* **2017**, *7*, 2755.
[13] P. Pietsch, M. Hess, W. Ludwig, J. Eller, V. Wood, *Sci. Rep.* **2016**, *6*, 27994.
[14] V. Vanpeene, A. Etiemble, A. Bonnin, E. Maire, L. Roué, *J. Power Sources* **2017**, *18*, 350.
[15] V. Vanpeene, J. Villanova, A. King, B. Lestriez, E. Maire, L. Roué, *Adv. Energy Mater.* **2019**, *9*, 1803947.
[16] V. Vanpeene, J. Villanova, J.-P. Suuronen, A. King, A. Bonnin, J. Adrien, E. Maire, L. Roué, *Nano Energy* **2020**, *74*, 104848.
[17] J. A. Lewis, F. J. Q. Cortes, Y. Liu, J. C. Miers, A. Verma, B. S. Vishnugopi, J. Tippens, D. Prakash, T. S. Marchese, S. Y. Han, C. Lee, P. P. Shetty, H.-W. Lee, P. Shevchenko, F. De Carlo, C. Saldana, P. P. Mukherjee, M. T. McDowell, *Nat. Mater.* **2021**, *20*, 503.
[18] J. Wang, C. Eng, Y. K. Chen-Wiegart, J. Wang, *Nat. Commun.* **2015**, *6*, 7496.
[19] J. Wang, Y. K. Chen-Wiegart, J. Wang, *Angew Chem Int Ed* **2014**, *53*, 17, 4460.
[20] T. Li, X. Zhou, Y. Cui, M. L. Meyerson, J. A. Weeks, C. Buddie Mullins, V. De Andrade, F. De Carlo, Y. Liu, L. Zhu, *ChemSusChem* **2021**, *14*, 1370.
[21] Md. A. Rahman, X. Wang, C. Wen, *J. Electrochem. Soc.* **2013**, *160*, A1759.
[22] H.-F. Wang, Q. Xu, *Matter* **2019**, *1*, 565.
[23] D. Schröder, C. L. Bender, M. Osenberg, A. Hilger, I. Manke, J. Janek, *Sci. Rep.* **2016**, *6*, 24288.
[24] D. Schröder, T. Arlt, U. Krewer, I. Manke, *Electrochem. Commun.* **2014**, *40*, 88.
[25] T. Arlt, D. Schröder, U. Krewer, I. Manke, *Phys Chem Chem Phys* **2014**, *16*, 22273.
[26] R. Franke-Lang, T. Arlt, I. Manke, J. Kowal, *J. Power Sources* **2017**, *370*, 45.
[27] F. Sun, R. Gao, D. Zhou, M. Osenberg, K. Dong, N. Kardjilov, A. Hilger, H. Markötter, P. M. Bieker, X. Liu, I. Manke, *ACS Energy Lett.* **2019**, *4*, 306.
[28] Z. Su, V. De Andrade, S. Cretu, Y. Yin, M. J. Wojcik, A. A. Franco, A. Demortière, *ACS Appl. Energy Mater.* **2020**, *3*, 4093.
[29] B. Goris, W. Van den Broek, K. J. Batenburg, H. Heidari Mezerji, S. Bals, *Ultramicroscopy* **2012**, *113*, 120.
[30] G. Ding, Y. Liu, R. Zhang, H. L. Xin, *Sci. Rep.* **2019**, *9*, 12803.
[31] Y. Huang, S. Wang, Y. Guan, A. Maier, arXiv preprint: ArXiv200102469 [Cs-Eess-Stat].
[32] Y. Huang, T. Würfl, K. Breininger, L. Liu, G. Lauritsch, A. Maier, in *Med. Image Comput. Comput. Assist. Interv. – MICCAI 2018* (Eds.: A. F. Frangi, J. A. Schnabel, C. Davatzikos, C. Alberola-López, G. Fichtinger), Springer International Publishing, Cham, **2018**, pp. 145–153.
[33] Y. Huang, X. Huang, O. Taubmann, Y. Xia, V. Haase, J. Hornegger, G. Lauritsch, A. Maier, *Biomed. Phys. Eng. Express* **2017**, *3*, 035015.
[34] M. Xia, T. Liu, N. Peng, R. Zheng, X. Cheng, H. Zhu, H. Yu, M. Shui, J. Shu, *Small Methods* **2019**, *3*, 1900119.
[35] T. Schoonjans, A. Brunetti, B. Golosio, M. Sanchez del Rio, V. A. Solé, C. Ferrero, L. Vincze, *Spectrochim. Acta Part B At. Spectrosc.* **2011**, *66*, 776.
[36] B. L. Henke, E. M. Gulikson, J. C. Davis, in *Atomic Data and Nuclear Data Tables*, **1993**, pp. 181-342, 54, 2..
[37] B. L. Henke, *Filter Transmission Calculator* https://henke.lbl.gov/optical_constants/Filter2.html.
[38] F. Lepoivre, A. Grimaud, D. Larcher, J.-M. Tarascon, *J. Electrochem. Soc.* **2016**, *163*, A923.
[39] J. J. Bailey, T. M. M. Heenan, D. P. Finegan, X. Lu, S. R. Daemi, F. Iacoviello, N. R. Backeberg, O. O. Taiwo, D. J. L. Brett, A. Atkinson, P. R. Shearing, *J. Microsc.* **2017**, *267*, 384.
[40] D. Gürsoy, F. De Carlo, X. Xiao, C. Jacobsen, *J. Synchrotron Radiat.* **2014**, *21*, 1188.
[41] SegmentPy documentation:http://segmentpy.readthedocs.io.
[42] W. Walker, V. Giordani, J. Uddin, V. S. Bryantsev, G. V. Chase, D. Addison, *J. Am. Chem. Soc.* **2013**, *135*, 2076.
[43] J.-L. Shui, J. S. Okasinski, P. Kenesei, H. A. Dobbs, D. Zhao, J. D. Almer, D.-J. Liu, *Nat. Commun.* **2013**, *4*, 2255.

Manuscript received: June 7, 2021
Version of record online: January 27, 2022

© 2022 The Authors. Published by Wiley-VCH GmbH

26289725, 2022, 5, Downloaded from https://chemistry-europe.onlinelibrary.wiley.com/doi/10.1002/cmtd.202100051 by Université De Toulouse 3, Wiley Online Library on [20/06/2023]. See the Terms and Conditions (https://onlinelibrary.wiley.com/terms-and-conditions) on Wiley Online Library for rules of use; OA articles are governed by the applicable Creative Commons License